PAPER

Check for updates

Rhodamine based turn-on dual mode chemosensor for the selective recognition of nickel ions: practical and theoretical applications†

Priya Takkar,[a] Swati Negi,[a] Rita Kakkar [b] and Rakesh Kumar [*a]

This work presents the development of a rhodamine-based colorimetric and turn-on fluorescent chemosensor (**P1**) designed for selective recognition of Ni^{2+} ions. Chemosensor **P1** exhibited remarkable sensitivity and selectivity for Ni^{2+} ions, exhibiting clear colorimetric and fluorescence responses. The binding interactions were meticulously examined using UV-Vis. and fluorescence spectroscopy, demonstrating a 1:1 stoichiometric ratio between **P1** and Ni^{2+} ions *via* a Job's plot and Benesi–Hildebrand analysis, while the binding constant and limit of detection were established as 0.8919×10^4 M^{-1}, and 2.15 nM, respectively. Interference studies demonstrated that competing metal ions had a minimal effect on the selectivity of the sensor. Chemosensor **P1** showed practical applicability by fabricating paper strips and solid-state silica gel systems, facilitating the rapid and visible detection of Ni^{2+} ions. Their stability and effectiveness were confirmed under a wide range of pH conditions. A molecular INHIBIT logic gate was created utilizing Ni^{2+} and EDTA as inputs in conjunction with memory devices featuring a "write-read-erase-read" binary logic function, highlighting **P1**'s capabilities in logic-based sensing and data storage. Furthermore, **P1** demonstrated reversible binding to Ni^{2+} in the presence of EDTA, enhancing its versatility. Density Functional Theory (DFT) calculations offered valuable insights into the molecular interactions, while the analysis of actual juice samples confirmed the efficacy of **P1** for detecting Ni^{2+} in complex matrices, making it an exceptional candidate for advanced environmental and analytical sensing technologies with outstanding selectivity and versatility.

1 Introduction

The growing reliance on heavy metals in modern industries has triggered environmental concern.[1] The use of nickel is expanding in modern technologies owing to its unique physical and chemical characteristics.[2] Nickel compounds are employed in electroforming, electroplating, nickel–cadmium (Ni–Cd) and Ni-metal hydride (NIMH) batteries, electronic equipment such as electric motors, transformers, and data storage devices.[3–5] Nickel is also a crucial component in catalytic converters of automobiles, coins, and medical devices such as pacemakers, orthopedic implants, and dental appliances.[6,7]

Although nickel has numerous beneficial applications, its toxicity should not be overlooked. Acute exposure to nickel results in respiratory difficulties, skin irritation, and gastrointestinal distress.[8,9] Chronic nickel exposure, particularly *via* inhalation or ingestion of nickel compounds, has been

attributed to severe ailments, including dermatitis, lung fibrosis, and kidney and cardiovascular diseases.[10,11] Based on the augmented incidences of nasal and lung cancer among nickel mining, smelting, and refinery employees, epidemiological studies have conclusively linked nickel compounds as human carcinogens.[12,13] Nickel is also known to trigger hypoxic conditions as it could potentially substitute iron in a theoretical oxygen sensor, resulting in alterations in the cell's metabolism that resemble a persistent state of oxygen deprivation, known as hypoxia.[14,15] Nickel is classified as a toxic, non-essential heavy metal that can have detrimental effects on the environment and human health.[16] Hence, the capability to detect Ni^{2+} ions precisely and selectively is extremely critical for environmental monitoring and public health.

Over the years, the design and development of chemosensors that selectively respond to specific target analytes have revolutionized the field of analytical chemistry.[17–20] Chemosensors have multiple advantages over conventional analytical methods, including rapid response times, excellent sensitivity, and the potential for real-time monitoring[21,22] Consequently. Researchers have been actively investigating novel pathways for designing and synthesizing chemosensors for selective recognition of Ni^{2+} ions. Rhodamine-based chemosensors have attracted significant attention because of their outstanding

[a]*Bioorganic Laboratory, Department of Chemistry, University of Delhi, Delhi-110007, India. E-mail: rakeshkp@email.com*

[b]*Computational Chemistry Group, Department of Chemistry, University of Delhi, Delhi-110007, India*

optical properties, ease of functionalization, and the potential to undergo color and fluorescence alterations in the presence of particular metal ions.[23] Furthermore, the unique ability of rhodamine to reversibly transform from a nonfluorescent spirolactam form to a fluorescent ring-opened amide form makes it an appropriate candidate exhibiting exceptional "on/off" fluorescence signals upon binding with certain analytes.[24] These attributes make rhodamines attractive candidates for selective recognition of Ni^{2+} ions.

This study involved a thorough investigation of the design and development of a unique rhodamine-based chemosensor (**P1**) that exhibits remarkable selectivity, sensitivity, and versatility for Ni^{2+} ions in both colorimetric and fluorometric detection modes. The chemosensor demonstrated a clear color transition from colorless to pink, accompanied by a pronounced fluorescent "turn-on" response, facilitating both visual and fluorescence-based identification of Ni^{2+}. Furthermore, we investigated the capabilities of this chemosensor for developing molecular logic gates and memory devices, broadening its use beyond detection.

Chemosensor **P1** underwent additional validation *via* real-sample analysis, demonstrating its capability to successfully detect Ni^{2+} ions within complex food matrices. Furthermore, Density Functional Theory (DFT) analyses were utilized to elucidate the molecular interactions and electronic transitions that enhance sensor performance. Through a combination of experimental findings and theoretical perspectives, we seek to provide a thorough understanding of the sensor mechanism and its possible uses in environmental chemistry, analytical testing, and molecular electronics.

The implications of this study will provide valuable insights into advancements in chemosensing techniques for selective Ni^{2+} ion recognition, emphasizing the practical applications of chemosensor **P1** and paving the way for the creation of multifunctional molecular devices for future technological advancements.

2 Experimental

2.1 Materials and methods

All chemicals and solvents were of analytical grade and obtained commercially from Sigma-Aldrich and used without additional purification. Metal salts of various elements were obtained from reputable suppliers and were used in their original form. Stock solutions of metal salts were prepared using double-distilled water. The photophysical studies were conducted at room temperature. The compounds were purified by column chromatography using 100–200 mesh silica gel. Thin-layer chromatography (TLC) was performed on Merck silica gel 60 F 254 alumina-coated plates. Visualization was performed in a UV-Chamber. Melting point was measured using a Buchi M-560 instrument. NMR spectra were recorded in DMSO-d_6 on a JNM-EXCP 400 spectrometer (JEOL, USA) operating at 400 MHz for ^{1}H NMR and 100 MHz for ^{13}C NMR. The IR spectra were recorded using a PerkinElmer 2000 Fourier Transform Infrared spectrometer, whereas the HRMS data were obtained using an Agilent Technologies 6530 Accurate-Mass Q-TOF LC/MS Spectrometer. Absorption spectral studies were

conducted using a Cary Series UV-Vis spectrophotometer (Agilent Technologies), whereas fluorescence analysis was carried out using a Varian Cary Eclipse Fluorescence Spectrophotometer. Both instruments were used with a 1 cm quartz cuvette. A digital pH meter (Merck) was used to measure the pH.

2.1.1 Synthesis of thiophen-2-ylmethylene hydrazine (2). Thiophene-2-carbaldehyde (**1**; 1.0 mmol) was dissolved in 20 mL of ethanol in a 100 mL round-bottom flask. Hydrazine hydrate (1.0 mmol) was then added slowly under continuous stirring. To expedite the reaction, 1–2 drops of glacial acetic acid were added to the reaction mixture. The reaction mixture was refluxed for 5 h with continuous stirring at 80 °C. Once the reaction was complete, the mixture was cooled to room temperature and quenched with ice-cold water. The crude product was precipitated, collected by filtration, washed with cold ethanol, and dried under vacuum. The crude product was purified using column chromatography to obtain a pure yellow solid of **2** with an approximate yield of 92%.

2.1.2 Synthesis of 2-amino-3′,6′-bis(diethylamino)spiro [isoindoline-1,9′-xanthen]-3-one (4). Hydrazine hydrate (2.4 mmol) was added dropwise in ice condition to a stirred solution of Rhodamine 12 B (**3**, 1 mmol) in ethanol, accompanied by the addition of 1–2 drops of glacial acetic acid. The reaction mixture was then refluxed at 80 °C for a duration of 3–4 hours. The progress of the reaction was monitored by thin-layer chromatography (TLC) using a suitable solvent system. After the completion of the reaction, as demonstrated by TLC analysis, the mixture was allowed to cool to ambient temperature. The reaction mixture was extracted with chloroform and filtered through sodium sulfate to eliminate any residual water. Subsequently, the solvent was removed under reduced pressure, leading to the formation of crude product. This product was purified by column chromatography, to obtain a pink solid product **4** in 90% yield.

2.1.3 Synthesis of 2-((3′,6′-bis(diethylamino)-3-oxospiro [isoindoline-1,9′-xanthen]-2-yl)imino)acetaldehyde (6). In a 100 mL round-bottom flask, 2-amino-3′,6′-bis(diethylamino) spiro[isoindoline-1,9′-xanthen]-3-one (**4**; 1.0 mmol) was dissolved in 10 mL of ethanol. Subsequently, oxalaldehyde (**5**; 1.0 mmol) was added to this solution, along with the addition of 1–2 drops of glacial acetic acid. The reaction mixture was refluxed at 80 °C for 3–4 h with continuous stirring throughout the process. The progress of the reaction was observed by thin-layer chromatography (TLC) using an appropriate solvent system. Upon completion of the reaction, as evidenced by the TLC analysis, the mixture was allowed to cool to room temperature. The reaction mixture was extracted with chloroform and filtered through sodium sulfate to remove any residual water. The solvent was eliminated under reduced pressure, resulting in the formation of crude product. The final product **6** was obtained as a yellow solid in 74% yield by column chromatography.

2.1.4 Synthesis of 3′,6′-bis(diethylamino)-2-((2-(((E)-thiophen-2-ylmethylene)hydrazono)ethylidene)amino)spiro[isoindoline-1,9′-xanthen]-3-one (P1). Compound (**6**) was subsequently employed in the synthesis of chemosensor (**P1**). 2-((3′,6′-Bis (diethylamino)-3-oxospiro[isoindoline-1,9′-xanthen]-2-yl)imino)acetaldehyde (**6**; 1 mmol) was added to a solution

of thiophen-2-yl methylene hydrazine (**2**; 1.2 mmol) in ethanol. One to two drops of glacial acetic acid were introduced into the reaction mixture, which was subsequently refluxed at 80 °C for a duration of 3–4 hours. The reaction was observed using thin-layer chromatography, and upon completion, it was allowed to cool to room temperature. The reaction mixture was extracted with chloroform and subsequently filtered through sodium sulfate to eliminate any residual moisture. The substance was subsequently evaporated under reduced pressure and further purified by column chromatography, resulting in a pure yellow product **P1** in 78% yield: m.p. 234–236 °C. ^{1}H NMR (400 MHz, DMSO) δ 8.76 (s, 1H), 8.04 (d, J = 8.3 Hz, 1H), 7.95 (d, J = 7.7 Hz, 2H), 7.83 (d, J = 4.9 Hz, 1H), 7.62 (d, J = 7.4 Hz, 2H), 7.56 (s, 1H), 7.22–7.19 (m, 1H), 7.06 (d, J = 7.3 Hz, 1H), 6.43 (d, J = 8.9 Hz, 4H), 6.36 (d, J = 9.0 Hz, 2H), 3.31 (s, 8H), 1.08 (s, 12H). ^{13}C NMR (100 MHz, DMSO) δ 164.91, 160.16, 152.57, 149.18, 145.20, 138.34, 135.27, 128.89, 127.89, 124.25, 123.89, 121.47, 118.91, 112.02, 108.72, 104.60, 97.84, 88.56, 44.14, 12.87. Molecular formula: $C_{35}H_{36}N_6O_2S$; HRMS data: calculated mass $(M + H)^{+}$, 604.77; found, 604.77 (Scheme 1).

2.2 UV vis and fluorescence studies

All spectral investigations of chemosensor **P1** were performed at room temperature to maintain uniformity and prevent temperature-related fluctuations in the data. Stock solutions of several metal ions, including Al^{3+}, Hg^{2+}, Mg^{2+}, Cu^{2+}, Zn^{2+}, Sr^{2+}, Fe^{2+}, Fe^{3+}, Cd^{2+}, Co^{2+}, Ni^{2+}, Mn^{2+}, Pb^{2+}, Na^{+}, Li^{+}, and K^{+} were freshly prepared in double-distilled water at a molecular concentration of 10 mM. Similarly, a 1 mM stock solution of chemosensor **P1** was prepared in acetonitrile, which was selected for its compatibility with the sensor and established capacity to dissolve organic substances without altering their chemical characteristics. To preserve the precision and dependability of the collected data, new solutions were prepared for each experiment. For metal-ion binding investigations, the interactions between chemosensor **P1** and the metal ions were thoroughly analyzed using both colorimetric and fluorometric techniques. Each trial involved the meticulous addition of 30 µL of a 1 mM stock solution of chemosensor **P1** and 30 µL of a 10 mM metal ion stock solution to a quartz cuvette. The solutions were further diluted to a final concentration of 10 µM prior to spectral quantification.

2.3 Interference studies

Interference experiments were conducted to evaluate the selectivity of chemosensor **P1** for Ni^{2+} ions. The objective of these competitive binding experiments was to assess the effect of different metal ions on the binding characteristics of **P1** to
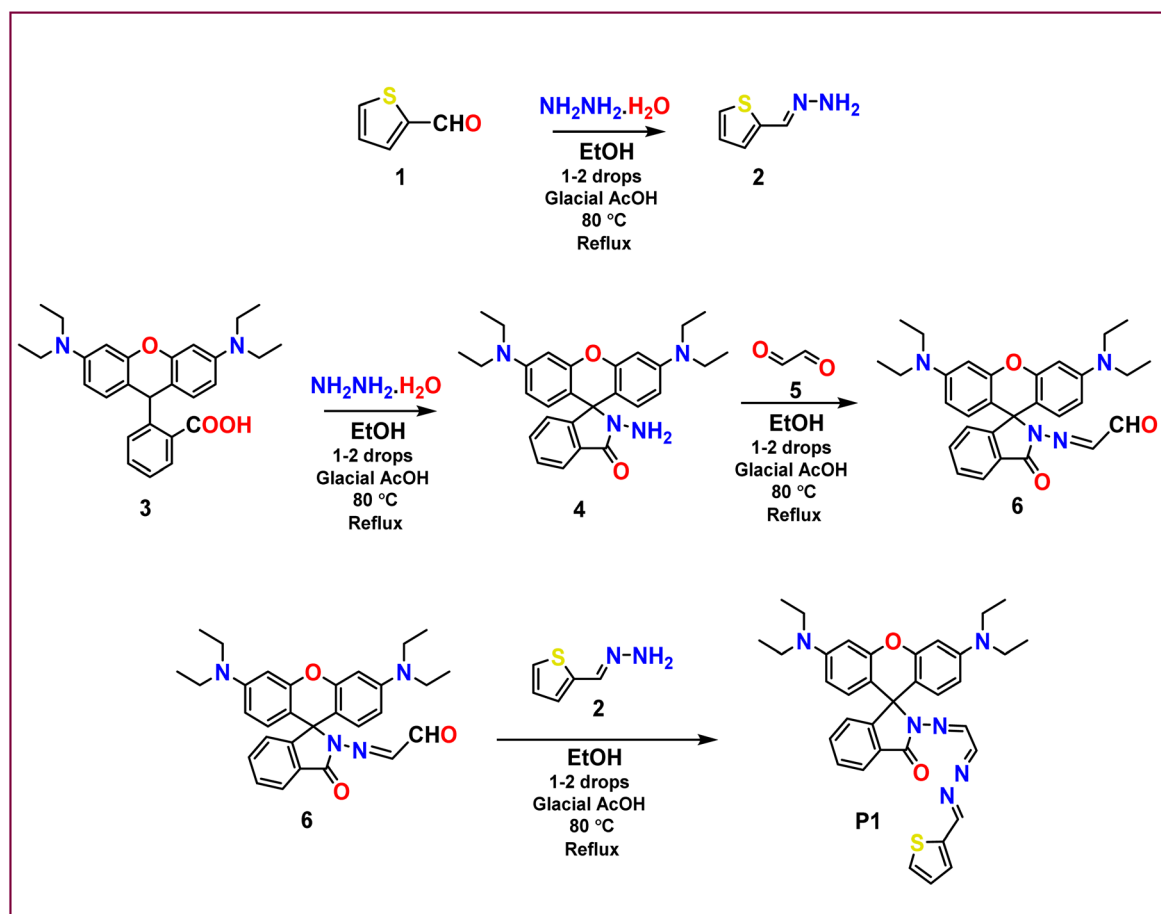
Scheme 1 Synthetic route for the synthesis of chemosensor **P1**.

Ni^{2+} ions. A 10 mM solution was prepared by combining 30 μL of each stock solution containing **P1** and Ni^{2+} ions in a quartz cuvette. Subsequently, 30 μL of stock solutions containing various metal ions were added sequentially to investigate the possible interference caused by these metals. All fluorometric spectra were obtained by excitation at 370 nm.

2.4   Job's plot measurements

The binding stoichiometry between **P1** and Ni^{2+} ions was determined by analyzing Job's plot measurements obtained from the fluorescence spectra. Freshly prepared acetonitrile solutions of **P1** (10 μM) and aqueous solutions of $NiCl_2$ (10 μM) were independently prepared. Job's plot measurements were conducted by varying the mole ratio of chemosensor **P1** from 0.1 to 0.9 keeping the combined volume of **P1** and Ni^{2+} ions in the range of 2 mL. Next, the solutions were diluted to a volume of 3 mL in a quartz cuvette to obtain the UV-Vis and fluorescence spectra at ambient temperature. Job's plots were generated by plotting the mole fraction of Ni^{2+} ($X_{Ni^{2+}}$) against $(F - F_o) \times X_{Ni^{2+}}$ at a wavelength of 589 nm. Here, F represents the fluorescence intensity at various ratios of **P1**–Ni^{2+}, whereas F_o represents the fluorescence intensity of **P1**.

2.5   Calculation of binding constant

Titration tests were performed by adding a 10 mM stock solution of Ni^{2+} (0–30 μL) to a solution containing 30 μL of 1 mM chemosensor **P1** in acetonitrile. Following each addition, the fluorescence spectra were measured to produce Benesi–Hildebrand (B–H) plots. The B–H plots were generated by plotting 1/$[Ni^{2+}]$ against $1/(I - I_0)$ for fluorescence emission spectra. Based on the slopes of these plots, the binding/association constant (K_a) was calculated using eqn (1).

$$\frac{1}{(I - I_0)} = \frac{1}{K_a(I_{max} - I_0)C} + \frac{1}{(I_{max} - I_0)} \quad (1)$$

Here, the fluorescence intensities in the presence and absence of Ni^{2+} ions are expressed by I and I_0. The binding constant (K_a) quantifies the equilibrium intensity of the interaction between chemosensor **P1** and Ni^{2+} ions, and C denotes the concentration of Ni^{2+} ions introduced throughout the titration process. I_{max} denotes the highest emission intensity recorded after the consecutive introduction of Ni^{2+} ions.

2.6   Limit of detection (LOD)

To assess the detection sensitivity of chemosensor **P1** for Ni^{2+} ions, we conducted ten replicate analyses of the blank solution (**P1**) to determine the standard deviation (σ). The following equation was used to establish the limit of detection (LOD):

$$\text{Limit of detection (LOD)} = \frac{3\sigma}{K_a}$$

where σ represents the standard deviation derived from the blank measurements and K_a denotes the binding constant established from the B–H plots.

2.7   Density functional theory studies

All the density functional calculations were performed using the DMol³ module[25–29] in Materials Studio. The Perdew–Burke–Ernzerhof (PBE) exchange–correlation functional was employed to accurately describe electronic interactions.[30] The PBE functional has been widely used for the balanced treatment of exchange and correlation effects. The double-numeric with polarization functions (DNP) basis set was chosen to ensure accurate representation of the electronic structure. This is a numerical basis set equivalent to the Gaussian 6-31G** basis set but is more accurate. We utilized DFT semi-local pseudopotentials (DSPP)[26] to describe the core electron interactions. Unrestricted density functional theory was used for open-shell systems comprising nickel ions and complexes. The integration accuracy was set to "fine."

Geometry optimization calculations were performed to determine the most stable configurations of the systems. No constraints were applied during the optimization. The atomic positions were allowed to relax until the force on each atom converged to less than 0.004 Ha $Å^{-1}$, the energy change was $<2.0 \times 10^{-5}$ Ha, and the maximum displacement was <0.005 Å. For self-consistent field (SCF) calculations, we employed a convergence criterion of energy change $<1.0 \times 10^{-5}$ Ha. These criteria ensured that the optimization reached a reliable solution. To confirm that the obtained structures were energy minima on the potential energy surface, we ensured that the Hessian matrix had no negative roots. The partial charges reported here are Hirshfeld partitioned charges.[31] The implicit solvent COnductor-like Screening Model (COSMO)[32,33] was used to study the solvent effect of acetonitrile ($\varepsilon = 37.5$).

2.8   Practical applications

2.8.1   Fabrication of paper strips. Whatman filter paper strips were immersed in a 1 mM acetonitrile solution of **P1** for 5 min to facilitate the uniform distribution of chemosensor **P1** across the strips, as illustrated in Fig. 1. Subsequently, they were dried under vacuum to yield a ready-to-use paper strip suitable for the recognition of nickel ions. Separate stock solutions (10 mM) of various metal ions were prepared. To evaluate the practical applicability of chemosensor **P1**, ready-to-use paper strips were submerged in various metal solutions, air-dried, and subsequently viewed by the naked eye and under a UV-chamber for colorimetric and fluorometric recognition, respectively.

2.8.2   Real sample analysis. To assess the detection of Ni^{2+} ions in actual samples, four distinct fruit and vegetable fruit juices (cucumber, tomato, orange, and apple) were sourced from a local market. Each sample type was analyzed using chemosensor **P1** to evaluate its effectiveness in identifying Ni ions (Ni^{2+}) in these food samples.

For fruit and vegetable juices, 5 mL of each juice was filtered to yield a clear extract solution, and subsequently diluted with distilled water to achieve a final volume of 25 mL. The diluted juices were infused with precise concentrations of nickel ions (Ni^{2+}). The spiked samples were analyzed using chemosensor **P1** without any additional pretreatment. Chemosensor **P1** was introduced into each sample, and the subsequent spectra were
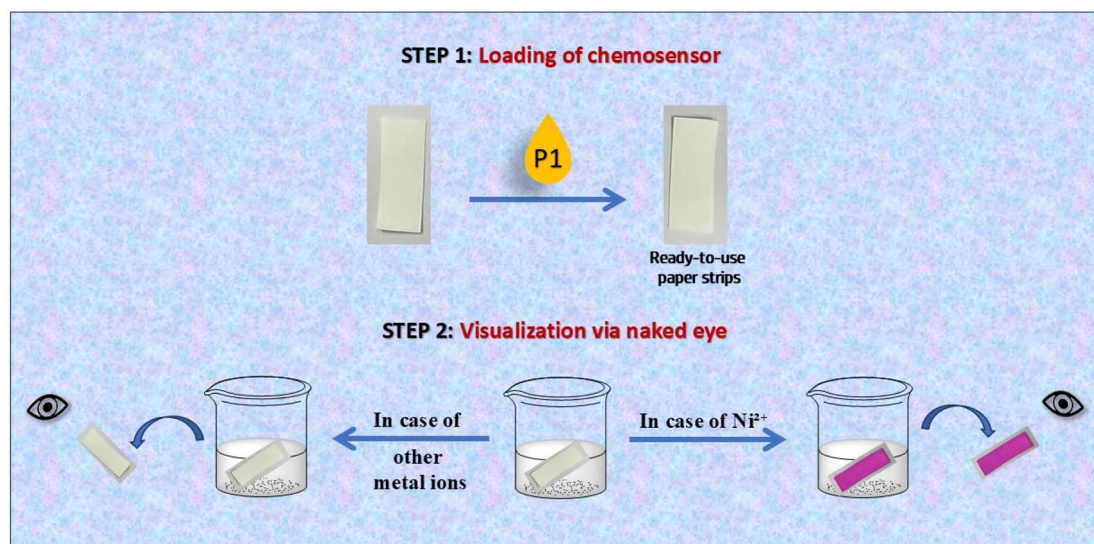
Paper

Fig. 1 Process of fabricating the paper strips coated with the synthesized chemosensor **P1** for visualizing nickel (Ni^{2+}) ions.

recorded. Aliquots of each juice sample were spiked with varying concentrations of Ni^{2+} ions, specifically from 1 to 100 μM, through the addition of a prepared Ni^{2+} solution. Fluorescence emission spectra were recorded for the spiked samples.

3   Results and discussion

3.1   Chemistry

Chemosensor (**P1**) was successfully synthesized by condensing 2-((3′,6′-bis(diethylamino)-3-oxospiro[isoindoline-1,9′-xanthen]-2-yl)imino)acetaldehyde (**6**) with thiophen-2-ylmethylene hydrazine (**2**) in ethanol. The reaction was initiated by the introduction of 1–2 drops of glacial acetic acid and conducted under reflux conditions at 80 °C for a duration of 3–4 hours. The final product was obtained as a pure-yellow compound by purification of the crude product using column chromatography, with a yield of 78%. The synthesized chemosensor exhibited a high yield and purity, indicating the effectiveness of the reaction conditions and purification steps. The successful synthesis of **P1** is important for subsequent investigation of its chemosensing properties.

3.2   Colorimetric response of chemosensor P1

The colorimetric response of chemosensor **P1** to Ni^{2+} ions was systematically examined to evaluate its sensing capability. Chemosensor **P1** was developed for selective interaction with Ni^{2+} ions and demonstrated a significant color change when exposed to these ions, suggesting its potential application for detecting Ni^{2+} in diverse samples. The introduction of Ni^{2+} ions into the acetonitrile solution of chemosensor **P1** resulted in a clear and quantifiable color shift. The acetonitrile solution of **P1** changed from colorless to pink upon interaction with Ni^{2+} ions, indicating the capacity of the chemosensor to change color in response to the presence of Ni^{2+} ions. The alteration in color was clearly observable by the naked eye in the case of the nickel ions, as illustrated in Fig. 2.

3.3   UV-vis spectral studies of chemosensor P1

The interaction of chemosensor **P1** with Ni^{2+} ions was examined by analyzing its UV-Vis spectral response. The UV-Vis absorption spectrum of chemosensor **P1** displays a broad absorption band at 323 nm, with no apparent absorption in the visible region. The observed spectral behavior was attributed to the closed spirolactam ring structure of the rhodamine moiety in **P1**, which was maintained in the absence of metal ions. The spirolactam form is characterized by its non-conjugated structure, resulting in a lack of light absorption in the visible spectrum, which maintains the colorless appearance of **P1** in solution.

Upon the gradual introduction of Ni^{2+} ions into the solution, a notable alteration in the UV-Vis absorption spectrum was observed. The intensity of the absorption band at 323 nm exhibited a progressive decrease, concurrent with the emergence of a new absorption band at 559 nm (Fig. 3), indicating the formation of a stable [**P1** – Ni^{2+}] complex. The observed spectral shift indicated a notable structural alteration in chemosensor **P1**, particularly the conversion from a closed spirolactam configuration to an open, conjugated structure. The alteration in the absorption spectrum, along with the

Fig. 2 The observable alterations in color of **P1** (10 μM, CH_3CN, pH 7.0) following the addition of 1 equivalent of different metal salts.
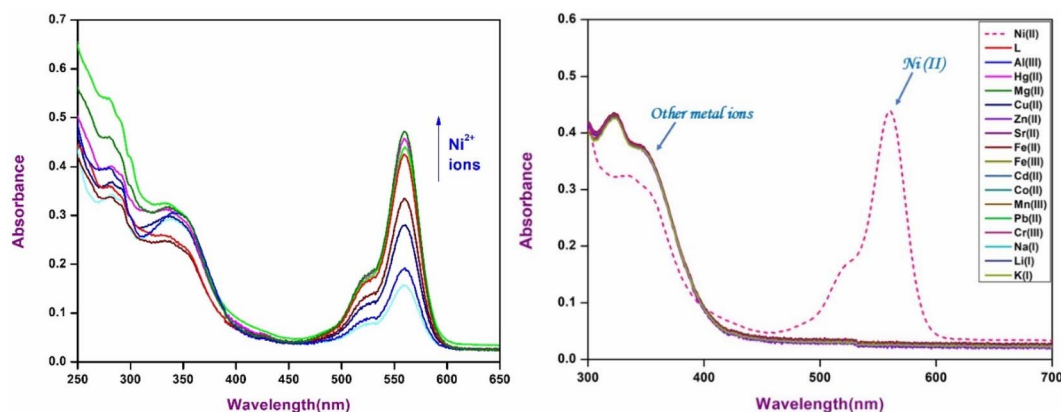
Fig. 3 (a) Changes in the UV-Vis spectra of **P1** (10 μM, CH$_3$CN, pH 7.0) upon the addition of 1 equivalent of different metal ions. (b) Absorption spectra of **P1** (10 μM, CH$_3$CN, pH 7.0) upon the sequential addition of Ni^{2+} ions.

observable color change, validates successful chelation and ring-opening reactions. The observed intense pink color was due to the high extinction coefficient of the rhodamine-type intermediate in the visible wavelength range. The colorimetric response indicates the efficient chemosensing ability of **P1** for Ni^{2+} ions, positioning it as a viable option for the detection of Ni^{2+} in diverse applications.

3.4 Fluorescence spectral response of chemosensor P1

The fluorescence characteristics of chemosensor **P1** were examined in acetonitrile solution containing various metal ions. Chemosensor **P1** exhibited no significant emissions when excited at 370 nm. However, upon the introduction of Ni^{2+} ions, pronounced band enhancement was observed at 586 nm, which was attributed to the transformation of spirolactam into the amide form (Fig. 4). A gradual increase in the fluorescence intensity was observed with the incremental addition of Ni^{2+} ions, indicating the strong binding affinity of **P1** for Ni^{2+} ions and the establishment of a stable [**P1** – Ni^{2+}] complex. However, the remaining metal ions did not result in any significant change in the fluorescence intensity of **P1**, demonstrating the highly selective affinity of **P1** for Ni^{2+} ions. The introduction of Ni^{2+} ions into the **P1** solution resulted in significant transformation. The Ni^{2+} ions form a chelate complex with the **P1** molecule, resulting in a chemical reaction that facilitates ring opening of the spirolactam structure of **P1**. The ring-opening process of the spirolactam structure in **P1** is crucial for its role as a chemosensor, especially for the detection of metal ions, such as Ni^{2+}. In its closed form, **P1** exhibits nonfluorescent properties and is colorless, displaying minimal visible absorption characteristics. When Ni^{2+} binds, the spirolactam ring opens *via* a chelation mechanism, in which Ni^{2+} coordinates with electron-donating sites on **P1**, resulting in weakening of the C–N bond. This reaction converts **P1** into a conjugated rhodamine-type structure, leading to significant absorption within the visible spectrum and distinct pink coloration. The improved conjugation facilitated fluorescence, enabling **P1** to be effective for both the colorimetric and fluorescent detection of Ni^{2+}.

3.5 Interference and competition studies

The specificity and selectivity of chemosensor **P1** for Ni^{2+} ions were assessed through interference and competition studies involving various competing metal ions, such as Al^{3+}, Hg^{2+}, Mg^{2+}, Cu^{2+}, Zn^{2+}, Sr^{2+}, Fe^{2+}, Fe^{3+}, Cd^{2+}, Co^{2+}, Ni^{2+}, Mn^{2+}, Pb^{2+}, Cr^{3+}, Na$^+$, Li$^+$, and K$^+$. Chemosensor **P1** was first subjected to individual exposure to these ions, resulting in no notable color changes or fluorescence variations except for Ni^{2+}. This observation indicates that **P1** exhibits a high selectivity, primarily for Ni^{2+}.

To validate this selectivity further, equimolar concentrations of metal ions were introduced into a solution containing **P1** and Ni^{2+}. The fluorescence intensity of the **P1**–Ni^{2+} complex, as depicted in Fig. 5, exhibited minimal variation in response to the presence of other metal ions. The observed minimal interference indicated that **P1** retained a robust binding affinity for Ni^{2+} while maintaining its turn-on fluorescence response even in complex environments containing various metal ions. The ability of **P1** to selectively identify Ni^{2+} ions amidst potential interferents increases its practical applicability in environmental and analytical contexts, thereby affirming its reliability for sensitive detection of Ni^{2+}.

3.6 Time response and effect of pH

The performance of **P1** was systematically evaluated over different time intervals and a broad pH spectrum using fluorescence emission techniques. The time-dependent behavior of **P1** in both the absence and presence of Ni^{2+} ions, was monitored to evaluate its response efficiency and stability. Fig. 6 shows that chemosensor **P1** displayed a nearly immediate response to Ni^{2+} ions, reaching equilibrium within minutes of exposure. The swift response demonstrates the sensor's elevated sensitivity, rendering it suitable for real-time detection of Ni^{2+} ions. In addition, the **P1**–Ni^{2+} complex exhibited remarkable stability over time, preserving consistent fluorescence measurements without notable degradation or variations. The stability of this system is essential for applications requiring long-term monitoring, because it guarantees
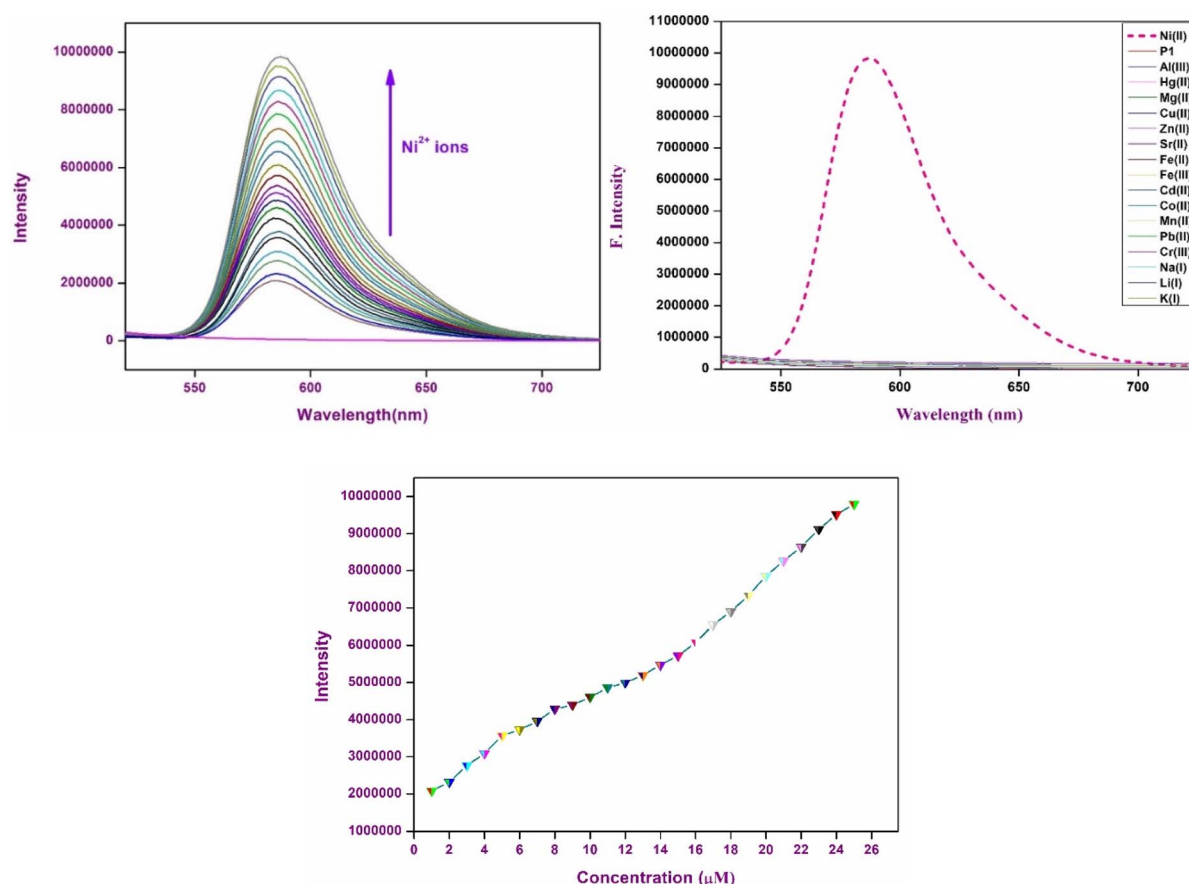
Fig. 4 (a) Changes in fluorescence spectra (λ_{max} = 586 nm) of **P1** (10 μM, CH$_3$CN, pH 7.0) upon the addition of 1 equivalent of different metal ions. (b) Fluorescence spectra (λ_{max} = 586 nm) of **P1** (10 μM, CH$_3$CN, pH 7.0) upon the sequential addition of Ni^{2+} ions. (c) Linear fit showing increase in fluorescence spectra (λ_{max} = 586 nm) of **P1** (10 μM, CH$_3$CN, pH 7.0) upon the sequential addition of Ni^{2+} ions.

dependable detection over prolonged durations. The chemosensor demonstrated negligible spectral variation in the absence of Ni^{2+} ions, highlighting its selectivity for Ni^{2+}.

The influence of pH on the functionality of chemosensor **P1** was examined over a wide pH range (4–12) to establish optimal operational parameters for the detection of Ni^{2+}. In environments with a pH range of 6–8, characterized as acidic to neutral, **P1** demonstrated a significant increase in fluorescence emission. This phenomenon is linked to protonation of the spirolactam ring. Protonation leads to the opening of the ring structure, which increases conjugation within the rhodamine core, resulting in a more pronounced spectral response. Within this pH range, the introduction of Ni^{2+} ions significantly enhanced the fluorescence signals, resulting in a chemosensor that exhibited a high sensitivity to Ni^{2+} ions. At elevated pH levels, ranging from 9 to 12, a notable decrease in fluorescence was observed. This decrease could be attributed to the formation of Ni hydroxides under alkaline conditions. This phenomenon hindered the effective binding of Ni^{2+} to the chemosensor, thereby obstructing the formation of the **P1**–Ni^{2+} complex. Under strongly basic conditions, the metal-free chemosensor exhibited reduced fluorescence values, further suggesting that its efficacy was compromised outside the neutral

pH range. The optimal conditions for conducting fluorescence experiments were established at pH 7, which provided maximum sensitivity and stability for the detection of Ni^{2+}.

Chemosensor **P1** showed significant sensitivity to both time and pH, highlighting its strong performance and suitability for various environmental and analytical applications that require quick and precise detection of Ni^{2+} ions.

3.7 Binding reversibility studies

To comprehensively examine the reversibility of the binding interaction between chemosensor **P1** and Ni^{2+} ions, binding reversibility studies were conducted using EDTA as a competing ligand. Following exposure of chemosensor **P1** to Ni^{2+}, EDTA (10 mM) was added to the acetonitrile solution to assess whether the initial color and fluorescence of **P1** could be reestablished. These findings indicate a progressive decrease in both absorption and fluorescence intensity, along with a significant color transition from vibrant pink, which signified the presence of Ni^{2+}, to colorless. This change indicates that the binding of Ni^{2+} by **P1** can be reversed when EDTA is present, as EDTA attaches to Ni^{2+}, releasing **P1** and returning it to its initial state (Fig. 7). The observed recovery of color and fluorescence suggests that chemosensor **P1** has potential for regeneration and reuse in
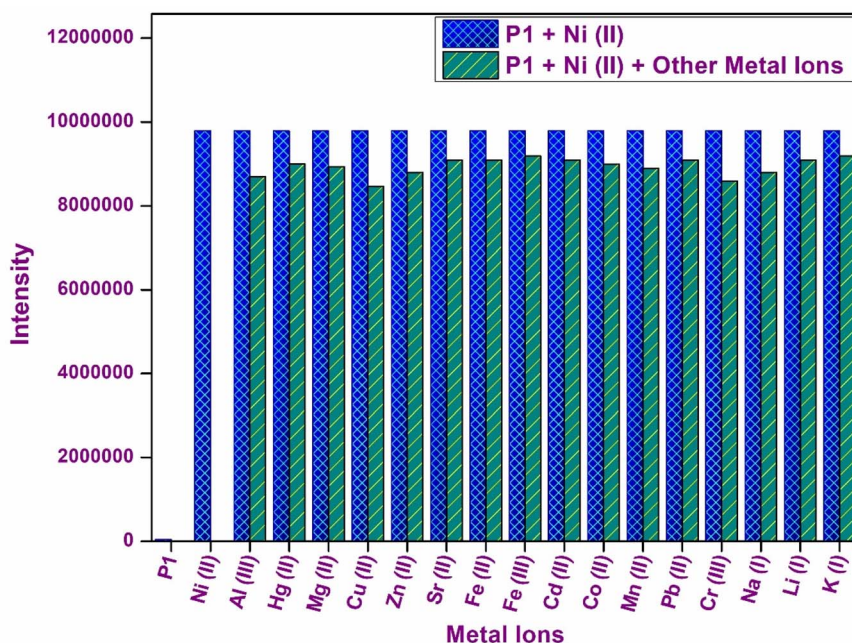
Fig. 5 Interference studies for Ni^{2+} ions analyzed *via* the fluorescence response of **P1** (10 μM, CH_3CN, pH 7.0) to several mixtures of different metal ions. The blue bars signify the inclusion of only Ni^{2+} ions to the **P1** solution while the green bars denote the alteration of the emission that occurs following the subsequent inclusion of other metal ions at $\lambda_{max} = 586$ nm.

future sensing cycles. This feature offers significant benefits for practical applications, enabling prolonged use of the chemosensor, which minimizes the necessity for frequent replacement and improves the operational durability. These reversible interactions establish **P1** as a strong candidate for the development of reusable chemosensors applicable to both environmental and analytical contexts.

3.8 Binding stoichiometry analysis

The binding stoichiometry between chemosensor **P1** and Ni^{2+} ions was meticulously assessed using Job's plot method, which involves systematically altering the ratio of chemosensor **P1** to Ni^{2+} ions while maintaining a constant total concentration. The

analysis demonstrated a 1:1 stoichiometric ratio, indicating that each molecule of **P1** associated with a single Ni^{2+} ion. The findings indicated a maximum at a mole fraction of 0.5, supporting the finding that a single Ni^{2+} ion coordinates with one **P1** molecule. This 1:1 binding stoichiometry was further confirmed by alterations in the fluorescence spectra, which consistently indicated the presence of a single binding site per chemosensor molecule. This stoichiometric relationship is crucial because it directly influences the sensitivity and specificity of chemosensor **P1** for Ni^{2+} detection.

In addition to stoichiometry, the binding constant (K_a) and limit of detection (LOD) were assessed using a Benesi–Hildebrand (B–H) plot, which demonstrated a linear correlation with
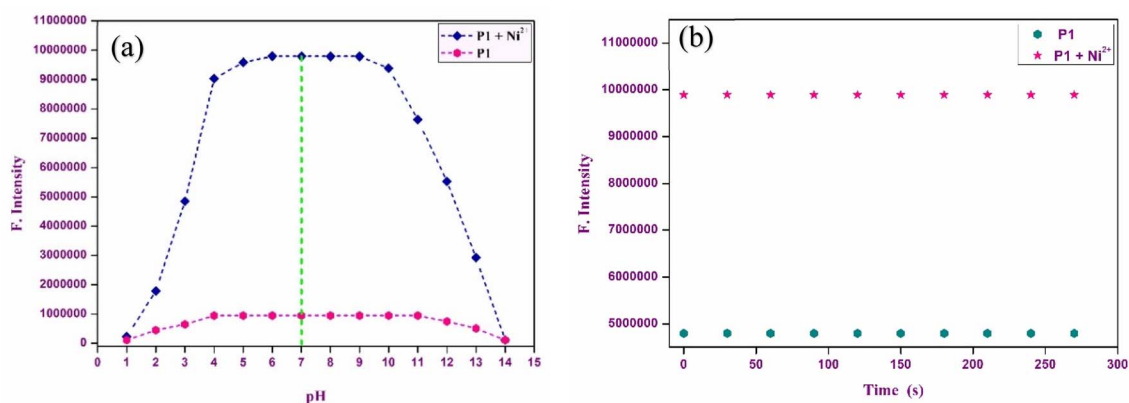

Fig. 6 (a) Time response studies of **P1** (10 μM, CH_3CN, pH 7.0) with Ni^{2+} ions at 586 nm. (b) Effect of pH on the fluorescence emission of **P1** and **P1**–Ni^{2+} complex at 586 nm.
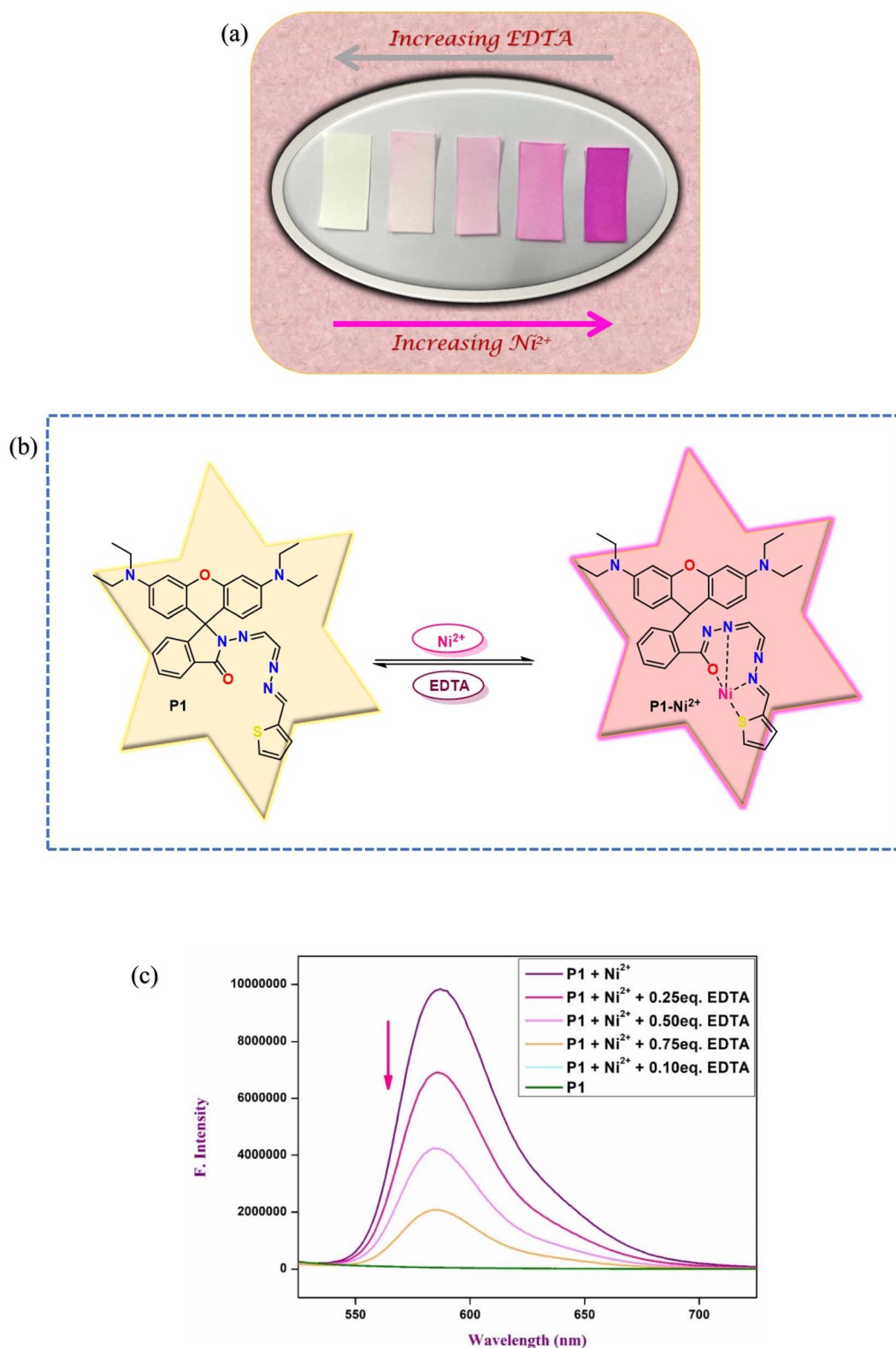
Fig. 7   (a) Strips immersed in an acetonitrile solution of P1 with escalating concentrations of Ni^{2+} and EDTA. (b) Plausible mechanism for the binding of P1 with nickel Ni^{2+} ions (c) reversibility of P1–Ni^{2+} complex upon the successive addition of EDTA.

the R^2 value close to unity, supporting the 1 : 1 binding model (Fig. 8). The pronounced linearity of the B–H plot facilitated the precise estimation of the binding constant (K_a), which was determined to be of the order of 0.8919×10^4 M^{-1}, signifying a robust affinity between P1 and Ni^{2+} ions. This significant binding constant highlights the ability of the chemosensor to
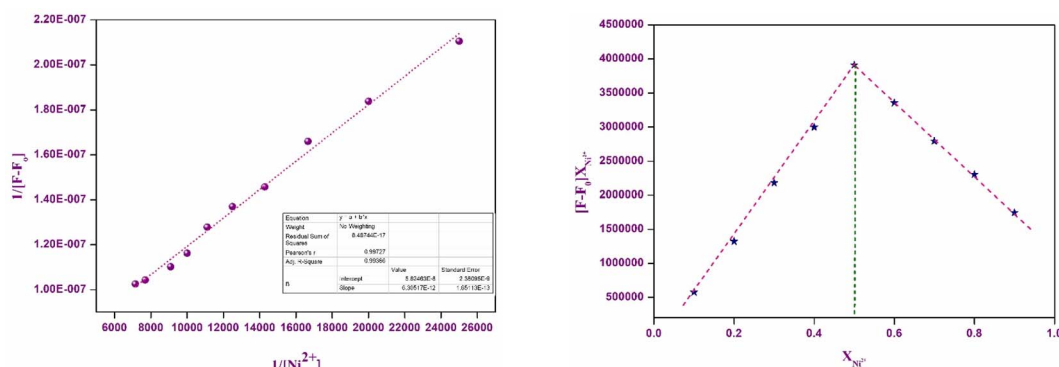
Fig. 8 (a) Benesi−Hildebrand (B−H) plot of **P1** with Ni^{2+} ions. (b) Job's plot of **P1** with Ni^{2+} ions.

detect Ni^{2+}. Furthermore, the limit of detection (LOD) was found to be 2.15 nM, offering important insights into the sensor's sensitivity and practical application in real-world contexts.

To enhance the performance of a chemosensor, it is essential to understand the precise 1 : 1 binding stoichiometry, which enables more precise quantification of Ni^{2+} ions in a variety of analytical applications. Table 1 emphasizes the performance of numerous chemosensors that have been reported in the literature for the detection of Ni^{2+} ions. The chemosensors presented below exhibit detection limits that range from 1.56×10^{-8} M to 5.59×10^{-6} M. The comparative values presented indicate improvements in sensitivity and the various responses recorded for nickel ions. The current research demonstrates that our chemosensor attains a detection limit of 2.15×10^{-9} M, highlighting its competitive performance and enhanced sensitivity. This result illustrates the sensor's capability for analysing real-world samples, especially in relation to previously published studies.

The specified stoichiometric ratio (1 : 1) increases the clarity and reliability of the sensor results, confirming its effectiveness as a reliable tool for detecting Ni^{2+} ions in environmental and analytical chemistry applications. The novelty and relevance of our work are now more explicitly established as a result of the comprehensive comparison.

3.9 Theoretical calculations

3.9.1 DFT studies

3.9.1.1 Chemosensor P1. As the experiments were performed using acetonitrile as the solvent, all computations were performed using this medium. The solvation energy of **P1** is -26.82 kcal mol^{-1}. The highest occupied molecular orbital (HOMO) and lowest unoccupied molecular orbital (LUMO) of **P1** are shown in Fig. 9. The HOMO is a π orbital of the xanthene ring, whereas the LUMO is a π^* orbital that lies primarily on the isoindoline ring and the conjugated bridge. The energy difference between the HOMO and LUMO influences nonlinear optical (NLO) characteristics. NLO performance improves when less energy is required for the transition from the ground state to the excited state. In the present case, the HOMO–LUMO gap

is quite small (1.331 eV), indicating that this molecule is highly reactive and likely to be an NLO material.

3.9.1.2 Ni-complex. Chemosensor **P1** reacted with nickel ions to form a complex. A plausible mechanism for Ni^{2+} binding to **P1** is shown in Fig. 7(b). DFT calculations were performed to verify the proposed mechanism.

Ni^{2+}, being a d^8 ion, can exist in either the singlet or triplet state. The multiplicity of the complex was examined. The ground-state SCF energies in the gas phase for the singlet and triplet states are -2424.027514 and -2424.004268 Ha, respectively, indicating that the ground state is a singlet *in vacuo*. The difference in energies is 14.59 kcal mol^{-1}. The solvation energies for the singlet and triplet states are -113.72 and -116.62 kcal mol^{-1}, respectively, so that the difference in energies decreases to 11.69 kcal mol^{-1} in acetonitrile solution. Nevertheless, the singlet state remains the ground state, both *in vacuo* and in the acetonitrile solution. The properties of the singlet state complex were examined in detail.

Fig. 10 shows the optimized geometry of the singlet state of the Ni(II) complex. The geometry of Ni is square-planar, binding to four atoms of the ligand: two nitrogen atoms, one oxygen atom, and one sulfur atom. When ligands are less demanding in terms of sterics, a square planar geometry is preferred[42] and the complex is diamagnetic; however, Ni complexes with bulkier ligands tend to form tetrahedral structures and are paramagnetic. The **P1**–Ni^{2+} complex is found to be square planar and diamagnetic. The computed complexation energy is -12.9 eV, confirming the strong affinity of chemosensor **P1** for nickel ions.

Fig. 11 shows the HOMO and LUMO contours of the complex. The HOMO is located on the xanthene ring, which is the electron-rich portion of the complex, whereas the LUMO is located on the nickel ion and the isoindoline ring. The HOMO–LUMO energy gap decreased from its value for **P1** to 0.737 eV, making the complex more reactive than the ligand.

The partial atomic charge on Ni was reduced to 0.0975 from 2. The electronic configuration of nickel in the complex was $[core]3\ s^{2.000}4s^{0.775}3p^{6.000}4p^{0.276}3d^{8.803}$, indicating that the ligand donated charges to the 4 s, 4p, and 3d orbitals of nickel. As shown in Fig. 9, the isoindoline ring is an electron-rich region in **P1**. Upon complexation with Ni^{2+}, it donates
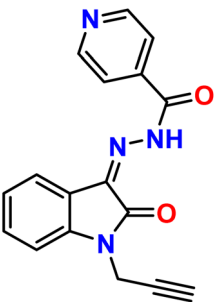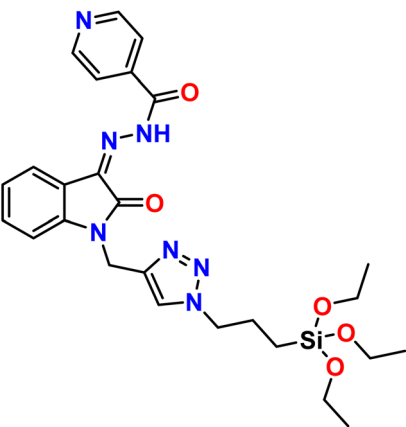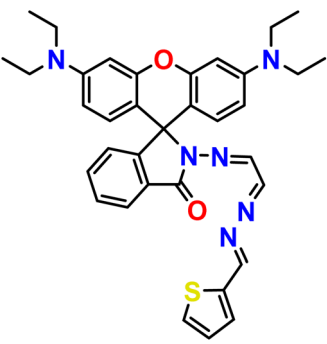
Table 1 Comparison of sensing capabilities of various chemosensors reported in literature with the present work

S. no.	Chemosensors	Ions detected	Binding stoichiometry	Detection limit (M)	Detection type	Ref.
1		Ni^{2+}	1 : 1	0.33×10^{-6}	Fluorescence	34
2		Ni^{2+}	1 : 1	0.29×10^{-6}	Fluorescence	31
3		Ni^{2+}	1 : 1	0.5×10^{-6}	Absorbance	35
4		Ni^{2+}	2 : 1	5.59×10^{-6}	Absorbance	36
5		Ni^{2+}	1 : 1	3.2×10^{-7}	Absorbance	37
6		Ni^{2+}	1 : 1	0.2×10^{-6}	Absorbance	38
7		Ni^{2+}	1 : 1	0.209×10^{-6}	Absorbance	39
8		Ni^{2+}	1 : 1	0.48×10^{-6}	Absorbance	40

Table 1 (*Contd.*)

S. no.	Chemosensors	Ions detected	Binding stoichiometry	Detection limit (M)	Detection type	Ref.
9		Ni^{2+}	1 : 1	2.49×10^{-7}	Absorbance	41
10		Ni^{2+}	1 : 1	1.56×10^{-8}	Absorbance	41
11		Ni^{2+}	1 : 1	2.15×10^{-9}	Absorbance and fluorescence	This work

electron density to the nickel ion, decreasing its negative charge and becoming electron deficient, as is evident from its participation in the LUMO of the complex (Fig. 11).

In our previous research on urease,[43] we found that hydroxamic acids are strong inhibitors of this enzyme owing to their chelating abilities. They bind to the Ni(II) centers in the active sites of urease in their anionic form *via* the (O,O) coordination mode. The Ni(II) centers in the urease active site are electrophilic, leading to significant charge transfer from the nucleophilic oxygen centers of the hydroxamate ligand to the Ni(II) centers upon binding to the active site. Similar charge transfer from the electron-rich isoindoline group was observed in this case.

3.9.2 Molecular logic gate application. The INHIBIT molecular logic gate employing chemosensor **P1** was developed to investigate the capabilities of molecular systems in executing logic operations through selective inhibition by particular inputs. This molecular logic gate configuration utilizes chemosensor **P1**, which operates in accordance with the principles of NOT, AND logic functions and responds to metal ions and anions, including Ni^{2+} and EDTA (Fig. 12).

To construct the INHIBIT logic gate, we employed two input categories: Ni^{2+} and EDTA. The response of chemosensor **P1** to these inputs was observed *via* its fluorescence emission at a wavelength of 586 nm, where a high emission intensity signified an 'ON' state and a low emission intensity indicated an 'OFF' state.

In the absence of Ni^{2+} and EDTA, the emission intensity of **P1** diminished, indicating an 'OFF' state. The presence of only Ni^{2+} resulted in a notable increase in emission intensity, indicating

$$\varepsilon_{HOMO} = -4.657 \text{ eV} \qquad \varepsilon_{LUMO} = -3.326 \text{ eV}$$
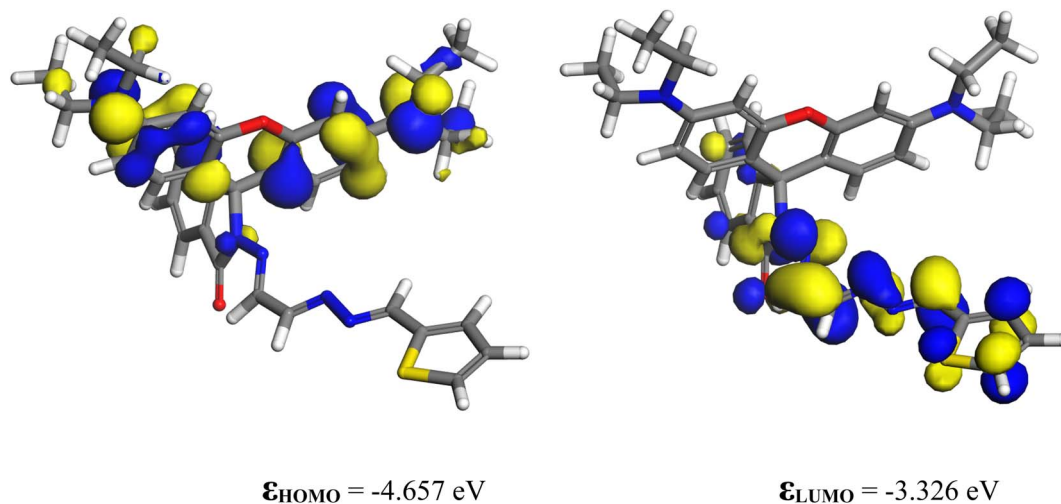
Fig. 9   The HOMO and LUMO of **P1**.

the 'ON' state. Nonetheless, the introduction of EDTA alone led to a significantly weak emission signal, indicating an 'OFF' state. This behavior indicates that the presence of EDTA suppressed the fluorescence signal, which corresponded to the NOT logic function.

The integration of these two inputs produced a fascinating outcome: the presence of both Ni^{2+} and EDTA resulted in a decrease in the emission intensity, indicating an 'OFF' state. This result validates the functionality of the INHIBIT gate, demonstrating that the presence of EDTA effectively suppresses the emission signal despite the presence of Ni^{2+}. The observed behavior aligns with the truth table for an INHIBIT gate, indicating that it is possible to construct an INHIBIT logic gate through the stepwise integration of these two inputs.

The successful implementation of the INHIBIT logic gate with chemosensor **P1** underscores its potential for application in intricate molecular logic systems, showing its capability to execute selective logic operations contingent on the presence of specific ions. This capability enables the development of advanced sensors and systems that respond specifically to various environmental and analytical conditions. Furthermore, the chemosensor **P1** demonstrated a reversible and reproducible colorimetric and fluorometric response following the sequential addition of Ni^{2+} (30 μM) and EDTA (60 μM) to its acetonitrile solution. A significant increase in fluorescence intensity was observed upon the addition of Ni^{2+}, which was later quenched by the addition of EDTA (Fig. 13).

3.9.2   Molecular memory device. Molecular memory devices represent an advanced strategy for data storage that employs molecular species as core components for data retention. Integrating these molecular components into sequential logic circuits enables the creation of systems that can execute intricate data-storage and retrieval tasks.

In this study, we created a molecular memory device utilizing chemosensor **P1**, showcasing a "write-read-erase-read" capability. This device employs emission intensity to encode binary states: a robust emission output at 586 nm indicates the 'ON' state (1), whereas a diminished emission output denotes the
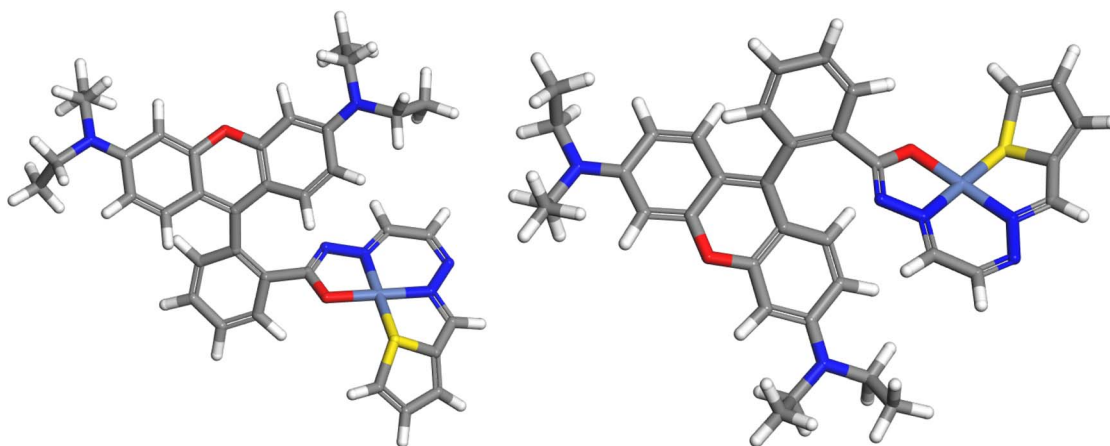

Fig. 10   Two views of the **P1**–Ni^{2+} singlet complex (color code: C – gray, H – white, N – dark blue, O – red, Ni – bluish-gray).
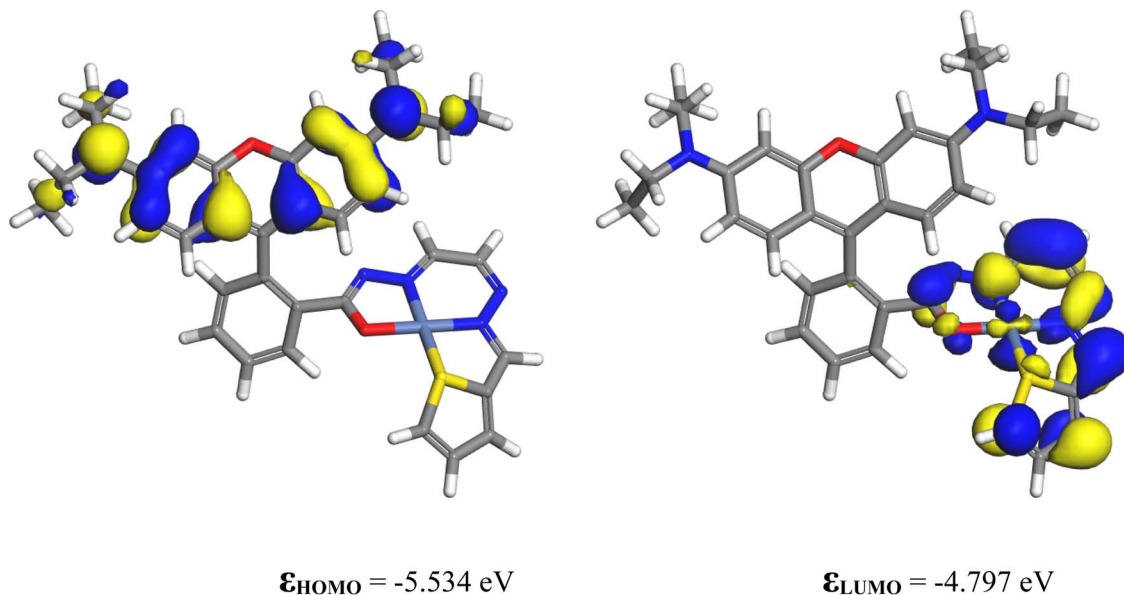
$$\varepsilon_{HOMO} = -5.534 \text{ eV} \qquad \varepsilon_{LUMO} = -4.797 \text{ eV}$$

**Fig. 11** The HOMO and LUMO of the singlet complex.

'OFF' state (0). To develop this memory device, we used two separate inputs: Ni^{2+} (A) for the SET process and EDTA (B) for the RESET process. Upon the introduction of input A (Ni^{2+}), **P1** demonstrates a significant emission intensity, effectively encoding and retaining the SET signal and binary state '1'. However, the introduction of input B (EDTA) served as a RESET signal, leading to a decrease in the emission intensity. This process effectively eliminates the previously stored data and establishes the binary state '0'.

This feature indicates the potential of the device to facilitate the creation of smaller and more economical integrated circuits. Moreover, the system demonstrated exceptional

stability and was capable of enduring numerous write-erase-write cycles without notable alterations in the emission intensity (as illustrated in Fig. 14). The consistency of this stability is essential to guarantee dependable and repeated utilization in real-world applications.

3.10 Practical applications

3.10.1 Fabrication of paper strips and solid state Ni^{2+} recognition. To investigate the practical applicability of chemosensor **P1**, we developed a test package that employs paper strips for colorimetric detection of Ni^{2+} ions. The paper strips were fabricated through a straightforward and efficient method,
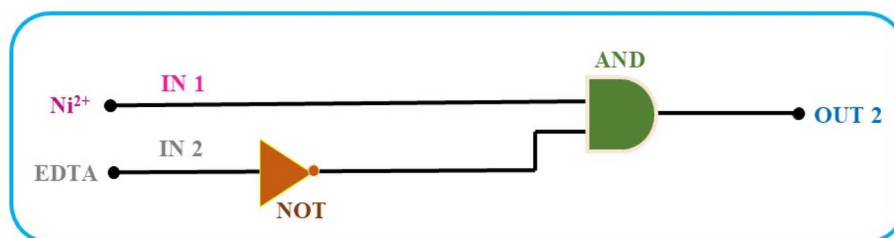
TRUTH TABLE

INPUT		OUTPUT
IN 1 [Ni^{2+}]	**IN 2 [EDTA]**	**OUT 2 ($F_{586 \text{ nm}}$)**
0	0	0
1	0	1
1	1	0
0	1	0

Fig. 12 Representation of the INHIBIT logic gate and its truth table based on Ni^{2+} and EDTA.
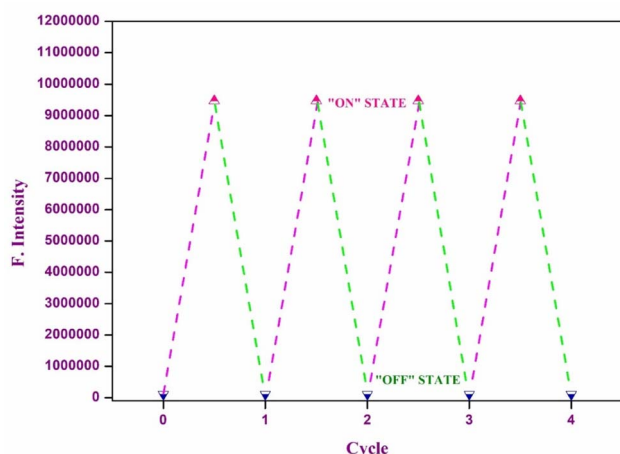
Fig. 13 The chemosensor **P1** shows reversible and reproducible fluorescence switching when Ni^{2+} and EDTA are added sequentially, indicating its potential use in molecular logic gate applications.

Fig. 15 The chemosensor test kit demonstrating the selective detection of nickel using **P1**-coated paper strips.

which included immersing them in an acetonitrile solution of chemosensor **P1** and subsequently allowing them to air-dry. The strips were tested with various metal ion solutions, such as Al^{3+}, Hg^{2+}, Mg^{2+}, Cu^{2+}, Zn^{2+}, Sr^{2+}, Fe^{2+}, Fe^{3+}, Cd^{2+}, Co^{2+}, Ni^{2+}, Mn^{2+}, Pb^{2+}, Na^+, Li^+, and K^+, to assess their specificity and sensitivity.

Upon exposure to Ni^{2+} ions, the **P1**-coated strips promptly displayed a distinct color change from colorless to pink, which was readily observable by the naked eye. The absence of this clear visual shift when the strips were immersed in solutions containing other metal ions confirmed the high selectivity of chemosensor **P1** for Ni^{2+} (Fig. 15). The ability to identify Ni^{2+}

without the influence of other ions underscores the potential of this paper-based test kit for targeted ion detection.

In addition to paper-based detection, solid-state detection of Ni^{2+} was successfully achieved using silica gel as a substrate for chemosensor **P1** (Fig. 16). Silica gel (100–200 mesh size) was initially combined with a 100 µM acetonitrile solution of **P1** and subsequently dried under reduced pressure to yield a colorless solid. Upon exposure to an acetonitrile solution containing Ni^{2+}
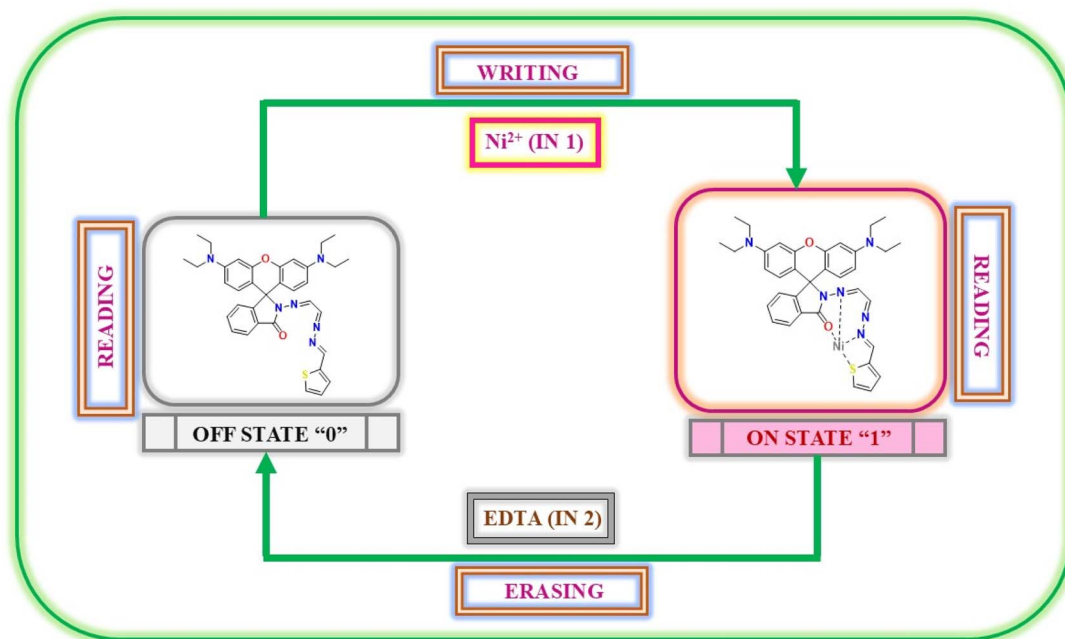

Fig. 14 Schematic illustration of the reversible logic-operation for the memory element featuring "write-read-erase-read" processes utilizing nickel ions and EDTA.

Fig. 16 Silica gel demonstrating a colorimetric and fluorescence response of **P1** to Ni^{2+} ions in a solid medium.

ions (100 μM), the **P1**-coated silica gel exhibited a rapid and striking transition from colorless to pink. This transformation further illustrates the robust colorimetric and fluorometric responses of **P1** when exposed to Ni^{2+}.

The paper strips and silica gel tests confirmed both the specificity and sensitivity of chemosensor **P1** while demonstrating its practical applicability in real-world scenarios. These findings indicate that **P1**-based test kits may function as practical and economical solutions for the rapid identification of Ni^{2+} ions across a range of environmental and analytical chemistry contexts. This straightforward nature, combined with the capacity for visual identification of Ni^{2+}, renders it exceptionally appropriate for field detection in settings without advanced laboratory facilities.

3.10.2 Real sample analysis. The analysis of real samples using chemosensor **P1** showed impressive capability for detecting nickel ions. The chemosensor demonstrated excellent recovery rates for spiked samples, demonstrating its reliability and accuracy in detecting Ni^{2+} ions in juice samples (Table 2).

The effectiveness of chemosensor **P1** was rigorously assessed using a spike-and-recovery method with actual juice samples

(cucumber, tomato, orange, and apple juice). To evaluate its efficacy, these samples were spiked with different concentrations of Ni^{2+} ions and subsequently analyzed using the newly developed assay. Each spiking and evaluation procedure was repeated five times to ensure precision and consistency. The spiked samples consistently demonstrated a significant increase in fluorescence quenching, indicating successful interaction between Ni^{2+} ions and **P1** within the constituents of the fruit juices. The findings, as outlined in Table 2, show remarkable efficacy in identifying and retrieving Ni^{2+} ions from the actual samples. This consistent and reliable detection emphasizes the appropriateness of chemosensor **P1** for the practical, visual identification of Ni^{2+} ions across various environmental and consumer settings, showcasing its potential for extensive use in monitoring and protecting against nickel contamination.

4 Conclusion

The synthesized rhodamine-based chemosensor **P1** demonstrated exceptional selectivity and sensitivity for the detection of Ni^{2+} ions both by colorimetrically as well as by fluorescence method. It shows a quick response time and stability within a slightly acidic to slightly basic pH range (pH 4–8). The 1 : 1 binding stoichiometry, as demonstrated by Job's plot and Benesi–Hildebrand analysis, highlights the sensor's reliability in detecting Ni^{2+} at a low detection limit (LOD = 2.15 nm; binding constant, $K_a = 0.8919 \times 10^4$ M^{-1}). Interference studies validated the specificity of **P1** for Ni^{2+} ions, demonstrating its applicability in detecting these ions in intricate environments. The impressive results for both solution and solid-state detection, as evidenced by the paper strip and silica gel applications, indicates their potential for practical implementation. Furthermore, **P1** exhibited reversible binding with Ni^{2+} in the presence of EDTA, significantly increasing its practical applicability and reusability. Molecular INHIBIT logic gate and memory device applications broaden the functionality of **P1** beyond traditional sensing, underscoring its potential for logic-driven and data-storage applications. Additionally, DFT analyses offered a significant understanding of the binding mechanism and electronic structure of the sensor, thus reinforcing the experimental results. The analysis of real samples confirmed the effectiveness of the sensor in environmental monitoring applications, providing a practical and economical solution for the detection of Ni^{2+} ions. Therefore, this study introduces **P1** as a highly sensitive, selective, and versatile chemosensor with potential applications in environmental and analytical chemistry, while laying the groundwork for the future advancement of rhodamine-based sensors that target other metal ions.

Data availability

Data will be made available on request.

Conflicts of interest

The authors declare no conflicts of interests.

Table 2 Determination of Ni^{2+} ions spiked into various samples of fruit juices using the synthesized chemosensor **P1**

Sample	Ni^{2+} ions spiked (μM)	Ni^{2+} ions found ($n = 5$)	Recovery of Ni^{2+} ions added (%)
Cucumber juice	5	4.94	98.8
	10	9.99	99.9
	15	14.02	93.5
	20	19.74	98.7
Tomato juice	5	4.74	94.8
	10	9.86	98.6
	15	14.90	99.3
	20	19.65	98.3
Orange juice	5	4.86	97.2
	10	9.84	98.4
	15	14.96	99.7
	20	20.10	100.5
Apple juice	5	5.01	100.2
	10	9.99	99.9
	15	14.92	99.5
	20	19.99	99.95

Acknowledgements

References

1 V. Masindi and K. L. Muedi, *Heavy Met.*, 2018, **10**, 115–133.
2 M. H. Ibrahim, D. Batstone, J. Vaughan and K. Steel, *Sep. Purif. Technol.*, 2024, **336**, 126291.
3 A. K. Shukla and B. Hariprakash, in *Encyclopedia of Electrochemical Power Sources*, ed. J. Garche, Elsevier, Oxford, 2nd edn, 2025, pp. 625–633.
4 P. Bernard and M. Lippert, in *Electrochemical Energy Storage for Renewable Sources and Grid Balancing*, Elsevier, 2015, pp. 223–251.
5 Z. Zhu, T. Jiang, M. Ali, Y. Meng, Y. Jin, Y. Cui and W. Chen, *Chem. Rev.*, 2022, **122**, 16610–16751.
6 L. T. Peiro, G. V. Mendez and R. U. Ayres, *INSEAD Report*, Fontainebleau, Fr, 2011, p. 61.
7 B. K. Reck, D. B. Müller, K. Rostkowski and T. E. Graedel, *Environ. Sci. Technol.*, 2008, **42**, 3394–3400.
8 M. Garcés, T. Marchini, L. Cáceres, V. Calabró, A. M. Mebert, M. V. Tuttolomondo, T. Vico, V. Vanasco, F. Tesan, J. Salgueiro, M. Zubillaga, M. F. Desimone, G. Valacchi, S. Alvarez, N. D. Magnani and P. A. Evelson, *Toxicology*, 2021, **464**, 153020.
9 R. G. Henderson, J. Durando, A. R. Oller, D. J. Merkel, P. A. Marone and H. K. Bates, *Regul. Toxicol. Pharmacol.*, 2012, **62**, 425–432.
10 A. Duda-Chodak and U. Blaszczyk, *J. Elem.*, 2008, **13**, 685–693.
11 E. Nieboer, F. E. Rossetto and C. R. Menon, in *Metal ions in biological systems*, CRC Press, 2024, pp. 359–402.
12 K. Salnikow and A. Zhitkovich, *Chem. Res. Toxicol.*, 2008, **21**, 28–44.
13 G. Genchi, A. Carocci, G. Lauria, M. S. Sinicropi and A. Catalano, *Int. J. Environ. Res. Public Health*, 2020, **17**, 679.
14 W. Begum, S. Rai, S. Banerjee, S. Bhattacharjee, M. H. Mondal, A. Bhattarai and B. Saha, *RSC Adv.*, 2022, **12**, 9139–9153.
15 M. He, C. Zhou, Y. Lu, L. Mao, Y. Xi, X. Mei, X. Wang, L. Zhang, Z. Yu and Z. Zhou, *Oxid. Med. Cell. Longev.*, 2020, **2020**, 5406284.
16 A. Cuschieri, J. I. Azzopardi and R. Blundell, in *Heavy Metals in the Environment: Management Strategies for Global Pollution*, ACS Publications, 2023, pp. 117–133.
17 D. Cao, Z. Liu, P. Verwilst, S. Koo, P. Jangjili, J. S. Kim and W. Lin, *Chem. Rev.*, 2019, **119**, 10403–10519.
18 A. Karmakar, P. Samanta, S. Dutta and S. K. Ghosh, *Chem.–Asian J.*, 2019, **14**, 4506–4519.
19 S. Dutta, A. Sinelshchikova, J. Andreo and S. Wuttke, *Nanoscale Horiz.*, 2024, **9**, 885–899.
20 S. Dutta, S. Fajal and S. K. Ghosh, *Acc. Chem. Res.*, 2024, **57**, 2546–2560.
21 M. Vonlanthen and N. S. Finney, *J. Org. Chem.*, 2013, **78**, 3980–3988.
22 M.-C. Ríos, N.-F. Bravo, C.-C. Sánchez and J. Portilla, *RSC Adv.*, 2021, **11**, 34206–34234.
23 M. Wang, X. Liu, H. Lu, H. Wang and Z. Qin, *ACS Appl. Mater. Interfaces*, 2015, **7**, 1284–1289.
24 M. H. Lee, J.-S. Wu, J. W. Lee, J. H. Jung and J. S. Kim, *Org. Lett.*, 2007, **9**, 2501–2504.
25 B. Delley, *J. Chem. Phys.*, 1990, **92**(1), 508–517.
26 B. Delley, *J. Chem. Phys.*, 1991, **94**(11), 7245–7250.
27 B. Delley, *J. Chem. Phys.*, 2000, **113**(18), 7756–7764.
28 B. Delley, *J. Phys. Chem.*, 1996, **100**(15), 6107–6110.
29 B. Delley, *Phys. Rev.*, 2002, **66**(15), 155125.
30 J. P. Perdew, K. Burke and M. Ernzerhof, *Phys. Rev. Lett.*, 1996, **77**(18), 3865–3868.
31 F. L. Hirshfeld, *Theor. Chim. Acta*, 1977, **44**(2), 129–138.
32 A. Klamt and G. Schüürmann, *J. Chem. Soc.*, 1993, **5**, 799–805.
33 B. Delley, *Mol. Simul.*, 2006, **32**(2), 117–123.
34 V. Kumar, D. Singh, P. Kumar, G. Chaudhary, A. P. Singh and R. Gupta, *J. Mol. Struct.*, 2022, **1261**, 132901.
35 J. Jiang, C. Gou, J. Luo, C. Yi and X. Liu, *Inorg. Chem. Commun.*, 2012, **15**, 12–15.
36 S. Goswami, S. Chakraborty, M. K. Adak, S. Halder, C. K. Quah, H. K. Fun, B. Pakhira and S. Sarkar, *New J. Chem.*, 2014, **38**, 6230–6235.
37 N. A. S. Pungut, M. P. Heng, H. M. Saad, K. S. Sim, V. S. Lee and K. W. Tan, *J. Mol. Struct.*, 2021, **1238**, 130453.
38 A. K. Jain, V. K. Gupta, P. A. Ganeshpure and J. R. Raisoni, *Anal. Chim. Acta*, 2005, **553**, 177–184.
39 S. Moon, J. J. Lee and C. Kim, *J. Mol. Struct.*, 2023, **1282**, 135210.
40 S. Y. Lee and C. Kim, *Inorg. Chem. Commun.*, 2017, **77**, 6–10.
41 G. Singh, S. Gupta, H. Kaur, P. Markan, P. Mohit and B. Mohan, *Inorg. Chem. Commun.*, 2024, **163**, 112319.
42 V. Bachler, G. Olbrich, F. Neese and K. Wieghardt, *Inorg. Chem.*, 2002, **41**(16), 4179–4193.
43 R. Arora, U. Issar and R. Kakkar, *J. Mol. Graph Model*, 2018, **83**, 64–73.